Graphical Abstract

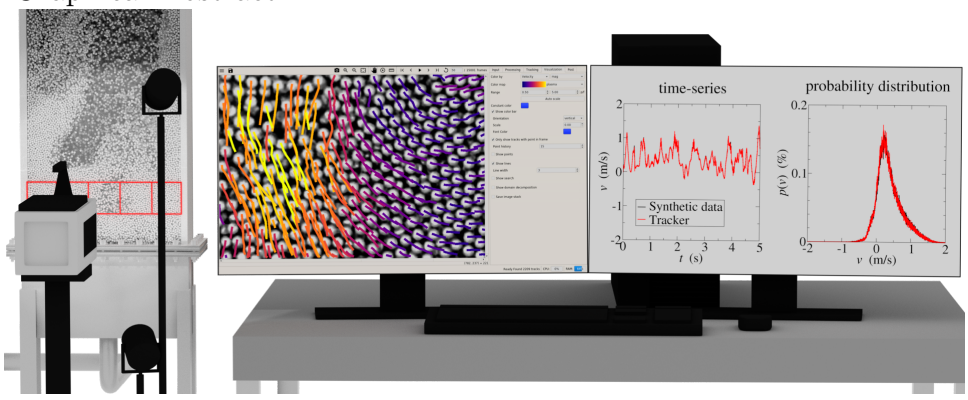

Critical analysis of velocimetry methods for particulate flows from synthetic data

Justin Weber[a], Jonathan E. Higham[b], Jordan Musser[a], William D. Fullmer[a,c,]

[a] *National Energy Technology Laboratory, Morgantown, WV 26507, USA*
[b] *University of Liverpool, School of Environmental Sciences, Roxby Building, Liverpool, United Kingdom, L69 7ZQ*
[c] *Leidos Research Support Team, Morgantown, WV 26507, USA*

Abstract

Particle tracking methods extract high-fidelity particle-scale velocity data from digital video measurements of particle laden flow. This experimental technique is often used to better understand the motion of particles and fluids in chemical processes and other complex particulate systems. Velocimetry measurements are also commonly used as benchmark data against which computational models are validated. However, the methods, codes, and experimental setups all have limitations. It is imperative that practitioners verify the velocimetry methods and their implementation as well as understand the limitations of experimental setups. This work focuses on quantifying the visible depth of field in a dense fluidized bed. Following a precedent set by the particle imaging velocimetry community, a particle velocity field is manufactured using a computational fluid dynamics and discrete element method simulation. Photo realistic high-speed videos are rendered based on

*Corresponding Author
Email address: william.fullmer@netl.doe.gov (William D. Fullmer)

the simulated data using the three-dimensional creation software Blender. Particle velocities are extracted from the synthetic high-speed videos using three variants of Particle Tracking Velocimetry and Optical Flow Velocimetry methodologies. The tracked results are then compared to the known solution, quantifying the error associated with the assumed visible depth. The results indicate that at a depth of one particle diameter, all three particle tracking codes give accurate measurements, largely within 5%. However, the error increases when the full bed video measurements are compared to the known solution at one particle diameter, i.e., mimicking a CFD validation study. For some statistics the constant depth assumption only increases the error slightly, for others significantly.
Keywords: velocimetry, particle, tracking, PTV, OFV, CFD-DEM, granular, multiphase, flow

1. Introduction

Gas-solid (particulate) fluidized beds are used in a variety of energy and chemical conversion devices due to their high interfacial transfer rates [1]. Collecting data in fluidized beds without intruding into the bed and affecting the flow can be challenging due to opacity of the particles. Some non-intrusive experimental methods exist which are able to measure particle-scale properties internally, namely positron emission particle tracking (PEPT), e.g., see [2–4], magnetic resonance imaging (MRI), e.g., see [5–7], and electrical capacitance tomography (ECT), e.g., see [8–10]. Yet, due to their ease of use, lower cost, and ability to produce high-quality data, velocimetry methods relying on digital images or high speed video (HSV) remain some of the most

commonly used techniques to study dense gas-fluidized [11–33] and granular [34–43] particle systems.

Velocimetry methods which extract particle position and speed from high speed video are frequently used because they may be applied to any device or section in which the internals may be imaged. This data is often treated as error free and potentially even used to calibrate models [44]. However, because the particles are most often opaque themselves, the imaging only captures a certain depth into particle-laden flows. Further, it is a variable depth which depends on the local particle concentration. Often this depth is approximated as a constant value, e.g., "[t]he depth of field was approximately 8 mm" [30], a number of particles, e.g., "[t]he depth of field of view was approximately one particle diameter," [22], or not approximated at all, e.g., "HSV imaging is taken to capture particle motion near the flat, front face of the bed" [32]. In reality, though, the depth of the field of view depends on the local hydrodynamics. In packed beds or dense emulsion regions of bubbling beds, the depth is effectively half a particle radius as the particles touching the wall obscure those behind them. In dilute transport flows or bubble regions of bubbling beds the effective depth depends on the lighting and the cameras' field of view, among other factors. There is a need to study this error in order to know how much confidence should be placed in velocimetry measurements of dense particle flows with solids concentrations greater than a few percent. In this work, we seek to quantify the level of error incurred by the uniform depth assumption, which is typically applied when post-processing CFD data to compare to the velocimetry data, i.e., for validation.

In order to make an error assessment, velocimetry results must be compared to known particle position and velocity data which cannot be obtained through traditional experimental measurements. Here, a non-trivial ground truth is constructed from numerical simulations using the commonly applied CFD-DEM method which explicitly resolves the motion and collisions of all particles in a system [3, 45, 46]. The numerical data are rendered into high-resolution, photorealistic high-speed videos (HSV) imitating an existing real-world setup. Three state-of-the-art, open-source tracking codes based on Particle Tracking Velcoimetry (PTV) and Optical Flow Velocimetry (OFV) are used to measure particle velocity from the synthetic HSV. We statistically evaluate the reliability of using HSV data at different internal depths to quantify the accuracy of the codes and the constant imaging depth assumption. An overview of the workflow is provided in Fig. 1.

The remainder of this work is organized as follows. In Sec. 2 the simulation method is briefly overviewed and the problem of interest, a bench-scale fluidized bed, is described. Section 3 discusses how the raw simulation data is rendered in to photorealistic HSV. Then, the velocimetry methods used to take measurements from the synthetic data are reviewed in Sec. 4. The velocimetry measurements are compared to the known simulated data in Sec. 5, which begins by defining several statistical measures used in the analysis. The work ends with a summary and outlook in Sec. 6.

2. CFD-DEM Simulation

Synthetic particle data is generated in this work using computational fluid dynamics (CFD) coupled with the discrete element method (DEM).

CFD-DEM is a common Euler-Lagrange numerical method for the simulation of gas-solids flows in which the particles are individually tracked, including collisions [3, 45], but not explicitly resolved by the continuum, unlike particle resolved direct numerical simulation (PR-DNS) [47]. The primary governing equations are provided in the Supplementary Material and readers unfamiliar with CFD-DEM are referred to, e.g., Zhu et al. [48], van der Hoef et al. [46], and Capecelatro and Desjardins [49] for a thorough description of the model equations. The open-source code MFiX (`https://mfix.netl.doe.gov`) is used for numerical solution of the governing equations. MFiX solves the gas-phase partial differential equations in a finite volume formulation in the style of Patankar [50] with a multiphase SIMPLE algorithm for pressure-velocity coupling [51]. Additional details of the numerical solution are also provided in the Supplementary Material.

In an effort to ensure that the synthetic data would represent real-world particle laden measurements, we choose to simulate an actual experiment where HSV was collected and used for velocimetry analysis. The National Energy Technology Laboratory's small-scale challenge problem (SSCP-I) [22] was selected to guide the formulation of the synthetic data used in this work. The SSCP-I experiment is simulated with a CFD-DEM model described below, similar to previous studies of the SSCP-I, primarily aimed at CFD validation [52–54].

The SSCP-I bed is a 3-inch (7.62 cm) deep by 9-inch (22.86 cm) wide rectangular channel with a modeled height of 121.92 cm. The particles have a diameter and density of $d_p = 3.256$ mm and $\rho_p = 1131$ kg/m^3. The total number of particles in the bed is $N_{tot} = 92948$. The gas is ambient air with

constant density, $\rho_g = 1.2$ kg/m^3, and viscosity, $\rho_g = 1.8 \times 10^{-5}$ Pa-s. The domain is discretized by a CFD grid of $36 \times 192 \times 12$ giving a uniform cell size of approximately $2d_p$. The coefficients of restitution (degree of inelasticity) for particle-particle and particle-wall collisions are 0.84 and 0.92, respectively. The Coulomb friction coefficients for both particle-particle and particle-wall collisions are 0.35. The spring constant of the linear spring dashpot model is set at $k_n = 2529$ N/m so that the collision time-scale is $\tau_{coll} = 2 \times 10^{-4}$ s. The timestep of the DEM subcycling is set at $\tau_{coll}/20$ and the maximum CFD timestep is limited to $5\tau_{coll}$. The experiment was operated at three flow conditions corresponding to inlet gas velocities of 2-, 3-, and 4-times the minimum fluidization velocity of $U_{mf} = 1.095$ m/s. This work focuses on the $U = 3U_{mf}$ condition.

In addition to bed pressure drop measurements, the SSCP-I experiment recorded HSV imaging of the particle dynamics at the front of the bed. Particle tracking was applied in five square averaging regions centered at an elevation of 7.62 cm. The edge of each bin is 4.572 cm in length so that the region of interest spans the width of the bed, see schematic in Fig. 2 and the Graphical Abstract. The original video is reported to have a pixel resolution of 1280 $\times$ 800 and that 22,000 frames were taken at rates between 1000 and 1500 frames/s (fps). The synthetic data is taken at the lower frequency of 1000 Hz and saved for a period of 25 s starting at 5 s to avoid any transient behavior due to initialization.

3. Synthetic Data Rendering

The open-source, 3-D creation software Blender (`www.blender.org`) is used to generate photorealistic images from the CFD-DEM simulations results. Specifically, Blender's physics based ray-tracing engine, Cycles, is used to render the scene in Fig. 2 which shows the modeled bed, near-wall particles, the camera and its orientation, as well as the region of interest (red boxes). The model bed contains opaque left and right side walls and clear acrylic front and back walls. A texture mimicking scratches is placed on the front acrylic wall to add noise and artifacts to the final rendering. Fig. 3(a) shows the cropped region of interest without particles, highlighting the photorealistic effects. Four high intensity light sources (lamps) were placed around the camera and positioned so that reflections from the acrylic were not observed. Although these lamps create harsh shadows, they are required to provide enough light to see the particles.

Using an in-house plug-in, the MFiX native particle positions are read directly into Blender. Each particle is represented as an ico-sphere, with two subdivisions and smooth shading. The synthetic Blender camera captures the same field of view as the SSCP-I experiment at the pixel resolution of 1280×800. In each dataset, 25,000 frames are rendered using two Nvidia Tesla P100s of the National Energy Technology Laboratory's high-performance computer Joule 2.0. The focal length of the synthetic camera is set at 55 mm with a 32 mm (width) image sensor. Camera distortion is simulated to ensure a fair representation of the experimental setup in the Blender rendering process. Example frames of the rendered images are provided in Fig. 3(b) and (c) showing only near-wall particles and all particles, respec-

tively. An example image of the actual, physical SSCP-I HSV is provided in Fig. 3(d) for comparison.

Finally, we note that a series of HSVs are rendered in an identical fashion from the same Blender scene that differ only in a pre-processing filter applied to the CFD-DEM simulation data. A sharp filter is used to mask particles beyond a set distance, $\mathcal{D}$, from the front wall. Depths of $\mathcal{D} = 1.5r_p$, $2r_p$, $3r_p$, $4r_p$, $6r_p$, $8r_p$, and 7.62 cm, the full bed depth ($\approx 46.8r_p$), are considered. All particles with centroid positions satisfying $z_p > \mathcal{D}$ are completely excluded from the rendering.

4. Velocimetry Methods

Two different velocimetry techniques are used in this study: Particle Tracking Velocimetry (PTV) and Optical Flow Velocimetry (OFV). Three specific implementations, i.e., codes, of these techniques are applied:

- Tracker (`https://mfix.netl.doe.gov/tracker`) a PTV method written in Python running on Windows, Linux and MacOS.
- flowonthego (`https://flowonthego.org`) an OFV method written Objective-C running on Android and iOS.
- PTVResearch (`https://github.com/jonnyhigham/PTVResearch`) a hybrid PTV and OFV method written in Matlab running on Windows, Linux and MacOS.

All three codes are free and open-source and developed by the authors of this work. We note that this work is not intended to compare one particle tracking

code or technique against another. Rather, multiple codes and methods are used to help ensure the findings are not specific to a particular velocimetry technique nor code implementation.

4.1. Tracker

PTV is a conceptually simple algorithmic technique in which an image is fragmented into discrete, identifiable objects. An object's displacement is found by determining which of the identified objects in adjacent frames are the same. Then, the velocity is simply the product of the displacement and HSV frame rate. In practice, PTV is rather challenging because matching seemingly similar objects across frames is not trivial. Additionally, image processing remains a mix of art and science as algorithm parameters are commonly selected to make the results *"look better"* qualitatively.

As a representative PTV algorithm, Tracker, an open-source particle tracking application written in python, leveraging OpenCV [55], Numpy [56], and Scipy [57] libraries, is used. In this work, the HSVs are pre-processed by applying a Gaussian blur filter with a size of 3.0 and a sigma of 1.0 (pixels) to remove noise from the image. Next, OpenCV's contrast limited adaptive histogram equalization (CLAHE) with a tile size of 8.0 $\times$ 8.0 and a clip limit of 9.0 pixels is used to increase the contrast of the image. To actually identify the particles in the image, OpenCV's `SimpleBlobDetector` is used which performs a series of thresholds, in this case from 30 to 255, to binarize the image. Centroids are determined from the binarized images, with similar centroids from the different thresholds being grouped to form one blob (object). These blobs are then filtered based on their area (60 to 140 pixels) and circularity (0.7 to 1.0). These values were manually adjusted to match the

apparent area of the particles in the image, maximizing the labeled particles and minimizing erroneous labels.

With the particles labeled, the next step is to identify the same particle across multiple frames to determine their displacement and, hence, velocity. Tracker's poly-projection algorithm is applied for this purpose which adapts from point (zeroth-order), linear and higher-order polynomials as successive frames are added to a particle's track history to predict where it will occur in the next frame [58]. Some specifics of the poly-projection as implemented in Tracker and used in this work can be found in the Supplementary Material. Generally, we observe that the poly-projection algorithm performs well because the HSVs are rendered at a sufficiently high frame rate. On average, displacements are found to be smaller than the apparent radius of the particles (7-9 pixels) so that the closest object to the projected location is typically the correct particle.

4.2. flowonthego

While the methods are very different, OFV is conceptually similar to PTV in that there are essentially two primary steps involved: identifying objects and tracking them across frames. Unlike PTV, which identifies object centoids, OFV typically identifies "features" from the image gradients. In the OFV code used here, flowonthego, features correspond to eigenfeatures which are determined from a correlation matrix,

$$\mathbf{M} = \begin{bmatrix} {\Psi_x}^2 & \Psi_x \Psi_y \\ \Psi_x \Psi_y & {\Psi_y}^2 \end{bmatrix} \tag{1}$$

where $\Psi(x, y; t)$ is the pixel intensity and Ψ_x and Ψ_y are the intensity gradients in the x- and y-directions, respectively. Gradients are computed from a

smoothed field using a Gaussian kernel with a width of five pixels. Eigenfeatures are defined as regions where the eigenvalues of **M** are at least 0.01. The displacement of across frames is determined from the optical flow equation [59]

$$\Psi_t + u\Psi_x + v\Psi_y \cong 0 \ , \tag{2}$$

where Ψ_t is the partial derivative of pixel intensity with respect to time between image pairs and u and v are the velocities in the x- and y-directions. Equation (2) is solved in flowonthego by applying the Lucas-Kanade solution method [60, 61] with a 15 $\times$ 15 pixel neighborhood (see Supplementary Material for more detail).

4.3. PTVResearch

In addition to PTV and OFV, a hybrid of the two methods is also considered in PTVResearch. Like the PTV code Tracker, the hybrid OFPTV code uses OpenCV's `SimpleBlobDetector` to identify discrete objects. The "blobs" are filtered based on their area (60 to 140 pixels) and circularity (0.7 to 1.0). The centroids of the N blobs identified in each frame are substituted for the eigenfeatures and their displacements are determined using the same optical flow solution method of the OFV code flowonthego.

5. Results and Discussion

5.1. Post-processing

In this section we provide the general methods in which the large volume of simulation and velocimetry data are processed into more compact forms suitable for error analysis. Mimicking the procedure used in the original

SSCP-I experiment, the field of view is split into five square spatial regions (bins) spanning the width of the channel and into which particle data are averaged. The values computed from these bins are identified with subscripts 1 through 5 increasing from left to right. The 25,000 frame (25 s) video is decomposed into five 5,000 frame (5 s) "segments." The segments are treated independently and used to compute 95% confidence intervals (CIs) for calculated errors. Finally, all seven videos with sharp depths of field of $\mathcal{D} = 1.5r_p$, $2r_p$, $3r_p$, $4r_p$, $6r_p$, $8r_p$, and full are processed in the same manner. The particle velocity data is post-processed using two distinct methods outlined below in Sec. 5.1.1 and 5.1.2, and depicted visually in the Graphical Abstract. Ultimately, we will study six primary quantities of interest, for each of the two velocity components, in five spatial bins, using seven depth-dependent variations of the five different video segments for a total of 2100 *averaged* data points for each of the velocimetry methods. Hence, distilling the results of this study into simple metrics is a considerable challenge.

5.1.1. Time-series analysis

Let $N_{j,i}$ be the set of all particles contained in the the j-th spatial bin at time $t_i = 0.001i + 5.0s$ where $i \in [1,\ 5000]$ is the frame index of the $s \in [1,\ 5]$ video segment. Then the time-dependent, spatially-averaged particle velocity is given by,

$$w_{j,i} = \frac{1}{N_{j,i}} \sum_{p=1}^{N_{j,i}} w_p(t_i) \ ,$$

where w_p represents either the x or y particle velocity component. Due to the uniform time interval between frames, the time-averaged mean is simply

$$W_j = \frac{1}{\sum \phi_i} \sum_{i=1}^{5000} \phi_i w_{j,i} \ , \tag{3}$$

where ϕ is a masking function such that $\phi = 0$ if $N_{j,i} = 0$, and $\phi = 1$ otherwise. The time-averaged standard deviation is given by

$$w'_j = \sqrt{\frac{1}{\sum \phi_i} \sum_{i=1}^{5000} \phi_i \left(w_{j,i} - W_j\right)^2} \ , \ . \tag{4}$$

It is, of course, possible to compute higher-order statistics from the $w_{j,i}$ time-series, however, the time-averaged mean and standard deviation are by far the most common quantities studied in practice.

5.1.2. Probabilistic analysis

Again let $w_p(t_i)$ be the x- or y-velocity component of a p-th test particle or track occurring in the j-th spatial bin of the i-th frame. Now, instead of averaging $w_p(t_i)$ together with like particles (tracks) of same time frame as in Sec. 5.1.1, $w_p(t_i)$ is grouped with like particles (tracks) of similar velocity over all time frames. Normalizing by the total number of particles (track) gives a discrete velocity probability distribution function (PDF) for the j-th spatial bin of the s-th video segment. First, $w_{p,i}$ is rounded to the nearest discrete k-th velocity bin as

$$w_k = \lfloor w_{p,i}/\delta w + \Delta w + \delta w/2 \rfloor \ ,$$

where the half-width, Δw, and interval, δw, of the velocity distribution are chosen to be 10.0 and 0.001 m/s, respectively. The probability of k-th velocity

is incremented (by one) for each particle or track and normalized by the total counts in each spatial bin at the end of each time segment producing $p_j(w_k)$, the discrete velocity PDF. The expected value of the distribution is defined by

$$E_j(w_k) = \sum_{k=-\Delta W/\delta w}^{+\Delta W/\delta w} w_k \; p_j(w_k) \; . \tag{5}$$

Then using the expected value of Eq. (5),

$$\mu_{w,j} = E_j \left[w_k \right] \tag{6}$$

$$\sigma_{w,j} = E_j \left[(w_k - \mu_j)^2 \right] \tag{7}$$

$$\gamma_{w,j} = E_j \left[\left(\frac{w_k - \mu_j}{\sigma_j} \right)^3 \right] \text{ and} \tag{8}$$

$$\kappa_{w,j} = E_j \left[\left(\frac{w_k - \mu_j}{\sigma_j} \right)^4 \right] \tag{9}$$

are the mean, standard deviation, skewness and kurtosis of the $p_j(w_k)$ velocity distribution.

5.1.3. Instantaneous time-series error

We begin the analysis by simply comparing the spatially binned time-series results from the velocimetry analyses with the known CFD-DEM solutions. In order to provide a clean comparison, each velocimetry method is compared to the known data separately. Example plots are provided in the Supplementary Material for the first time segment at key depths of $\mathcal{D} = 2r_p$ and the full bed depth. Qualitatively, all three velocimetry methods appear to be in excellent agreement with the known solution at the near-face depth of $\mathcal{D} = 2r_p$. However, there are some noticeable discrepancies between the known and evaluated time-series at the full bed depth. By comparing the

near-face and full bed images, it is apparent that the measured result has changed little while the CFD-DEM solution itself has shifted. This indicates that the bulk behavior deviates from the near-wall behavior, which is largely what the velocimetry methods are able to measure due to a limited depth of field.

To begin quantitatively assessing the error in the velocimetry methods we first look at the instantaneous discrepancy between the measured velocities, $\tilde{w}_j(t_i)$, and the ground truth, $w_j(t_i)$, i.e., the velocities computed from the known CFD-DEM data. The instantaneous error of all five segments at a depth of $\mathcal{D} = 2r_p$ for the two velocities are collapsed into parity plots in Fig. 4. The parity plots also show the 1:1 line surrounded by $\pm 10\%$ discrepancy lines; it can be observed that much of the data falls within these bounds. Both velocities range from, roughly, -1 to 2 (m/s) and Fig. 4 does not show a strong correlation deviating from the 1:1 line, indicating the absence of a velocity-dependent error in the methods over the investigated range. Error plots of the local discrepancy, $\delta w = \tilde{w}_j(t_i) - w_j(t_i)$, provided in the Supplementary Material are also devoid of strong w_j-dependent trends.

The error plots and, to a lesser extent, the parity plots of Fig. 4 do not appear to be representative of the good qualitative agreement observed when the time-series are simply plotted against one another as in the Supplementary Material. This is largely due to the sheer volume of data, some 125,000 points per plot, causing the outliers to stand out visually. To further quantify the comparison shown in the parity and error plots, the magnitude of the instantaneous discrepancy, $|\delta_w|$, is ordered into a cumulative distribution function (CDF). We select the 95-th percentile, denoted δw_{95}, as a scalar

indicator of each distribution and provide their (absolute error) values in Table 1. For quantities of interest that range from, roughly, -1 to $+1$ m/s, it is reassuring that a vast majority (95%) of the data is accurately predicted to within a few cm/s.

5.2. Global time-series error

In this section, the time-averaging described in Sec. 5.1.1 is applied to determine the mean and standard deviation of each transient signal. In order to reduce each quantity of interest to a single scalar for each depth, we make use of an L2-norm defined by

$$L_2(\phi) = \sqrt{\frac{\sum_{j=1}^{5} (\tilde{\phi}_j - \phi_j)^2}{\sum_{j=1}^{5} \phi_j^2}} \tag{10}$$

where ϕ is a quantity of interest (e.g., U_j or v'_j) known from the CFD-DEM simulation and $\tilde{\phi}$ is a velocimetry calculation of the rendered video of the same data. The global error of the time-averaged mean and standard deviation of the time-series are presented as function of imaging depth, $\mathcal{D}$, in Fig. 5. The four plots show the same general behavior: the error is typically at a minimum at $\mathcal{D} = 2$ or 3 r_p, increases gradually with increasing $\mathcal{D}$, reaching a maximum at the full bed depth. Again, we note that the limiting full case is approximately $\mathcal{D} = 46.8r_p$ and the large increase causes the discontinuity between $\mathcal{D} = 8r_p$ and full bed depth. It is reassuring that the visual approximation of Gopalan et al. [22] that the camera observes approximately one particle diameter in depth, or $\mathcal{D} = 2r_p$, appears to be confirmed quantitatively by Fig. 5.

Although all of the particles are guaranteed to have an unobstructed view of the camera in the smallest imaging depth, $\mathcal{D} = 1.5r_p$, it does not minimize

the error. This is due to the significant "noise" caused by the starting and ending of tracks as particles move in and out of the imaging plane. Due to the sharp filter, particles in the rendered HSV instantaneously appear or disappear as their centroids cross into or out of the $\mathcal{D}$-plane. Overall, the error is acceptable, particularly at $\mathcal{D} = 2$ to 4 r_p where all velocity methods have an error below 10% for all quantities, many of only a few percent. However, judging by the excellent qualitative agreement observed in the instantaneous comparisons (see Supplementary Material), 10% in mean quantities may seem high. Further analysis of the data shows that this is simply a quality of the sum of the mean values being relatively small. Consequently, some of the largest error observed is for $L_2(U)$ simply because U is the smallest value among these four quantities of interest. Although this is certainly not a new finding, it may serve as an additional caution to run both experiments and simulations for a long period of time when quantities of interest fluctuate appreciably around relatively small mean values.

Finally, we comment on the error bars presented in Fig. 5 which show 95% confidence intervals computed using a simple t-test of the L2-norms of the five different segments. In almost all cases, the largest error bars occur at the full bed depth where the error is a convoluted measure of non-uniformity (in the z-direction) of the particle flow. Specifically, the instantaneous time-series comparisons show regions of agreement and obvious disagreement. In almost all of such regions of good agreement, the CFD-DEM full result also compares well with its own near-wall solution, i.e., the CFD-DEM result at $\mathcal{D} = 2r_p$. In other words, the particle flow is approximately 2-D in these instances. Hence, segments with substantial time periods of approximately 2-

D flow will, somewhat artificially, be in good agreement with the velocimetry measurements and, conversely, segments with relatively few time periods of 2-D flow will not agree well with the measurements computed from video with near-wall particles obstructing the field of view.

In a few cases, large error bars are also observed at small imaging depths. Further analysis has indicated that this is due to the sharp cut-off of particles in the imaging plane resulting in artificially high fragmentation of particle tracks. For example, in Tracker, if the particle disappears in the rendered image without meeting the required four consecutive points in the track, no velocities will be measured. However, the CFD-DEM still has velocity measurements for the three time instances before leaving the imaging plane. Similarly when solving of the optical flow equations in flowonthego and PTVResearch, when a particle in the subsequent frame is missing, the least squares method is still able find a solution. In this case, computing a velocity for a missing particle will most likely result in an artificial value, as the method may find a similar feature on a particle further away.

It has been observed that despiking the velocimetry results can have a significant effect on the results. For example, all of the flowonthego time-series output at the $\mathcal{D} = 1.5r_p$ imaging depth were despiked using the Goring-Nikora method [62]. Consequently the global error in the standard deviation of the transverse velocity decreased from $L_2(u') = 11.8 \pm 13.3$ % to just $L_2(u') = 4.0 \pm 0.8$ %. Although this post-processing step does improve the results slightly in several other cases, and significantly in this example case, despiking is not an implicit step (at least currently) in any of the three velocimetry tools and, quite frankly, likely would not have been applied here

in a blind setting, i.e., if the authors had not known the correct solution *a priori*. Hence, despiking of the velocimetry data is not applied in this work beyond this illustrative example. However, it has shown to be a useful tool for PTV and OFV analysis of particle laden videos, specifically in dilute cases where relatively short tracks and regions temporarily devoid of particles may be common.

5.3. Global probability distribution error

The same analysis applied to the time-series measurements can also be directly applied the the velocity probability distribution analysis using the L_2-norm defined by Eq. (10). The error in the mean and standard deviation of the measured distributions is provided in Fig. 6 as function of imaging cut-off depth, $\mathcal{D}$. Similar to the time-series analysis, there is a general increase in error with increasing $\mathcal{D}$. Often there is a minor up-tick at the smallest imaging depth, below a single particle diameter, due to the noise caused by the high frequency of particles entering and exiting the sharp cut-off plane. At $\mathcal{D} = 2r_p$ the error is acceptable with means under 10% and standard deviations under 5%. We note that the general $L_2(\mu_w) > L_2(\sigma_w)$ pattern is due to the near-zero mean of the distributions, i.e., $\mu_w < \sigma_w$. It is of minor note that, by comparing Fig. 6 to Fig. 5, we see a diminished increase in error at the full bed depth in the PDF analysis compared the time-series analysis. This finding is consistent with the intuitive understanding that the particle dynamics at different depths may visit the same phase space though not necessarily at the same time, an artifact of thin, "quasi-2D" system.

Because higher-order statistics of distributions are more intuitive than of time-series, skewness and kurtosis measures are also considered. The L_2-

norms of γ_w and κ_w are provided in Fig. 7 which, perhaps unsurprisingly, show the same general trend as the previous statistics. On average, there is more error in the skewness than the lower order statistics. However, the fourth order statistic, kurtosis, is predicted quite well. This could be, again, simply due to the normalization of the error; $|\kappa_w|$ is roughly an order of magnitude larger than $|\gamma_w|$ on average. One data point breaking the established trend is the large error, and larger error bar, in $L_2(\kappa_u)$ measured by flowonthego at a depth of $\mathcal{D} = 2r_p$. Further investigation of this dataset shows that the large global error is due to a relatively small number of singular discrepancies. We consider, for example, the kurtosis in the fifth bin of the fourth segment where the measured value is $\tilde{\kappa}_{u,5} = 24.9$ and the actual value is $\kappa_{u,5} = 7.66$. A qualitative comparison shows no obvious issues unless the PDFs are viewed in semi-log scale. As shown in the Supplementary Material, while the bulk of the distribution is well-captured, there are a handful of low probability, of $O(-6)$, points in the measured PDF which are null in the known PDF. When these points are eliminated (we set any $p(u) \leq 2 \cdot 10^{-6}$ to $p(u) = 0$ and re-normalize the distribution to unity), the measured kurtosis drops to $\tilde{\kappa}_{u,5} = 6.85$. Similar manipulation of the known distribution gives $\kappa_{u,5} = 6.48$, shrinking the relative error from over 200% to just 5% by removing just 0.02% of the cumulative distribution. While it may be straightforward to massage the data to give a better comparison, we would not have considered doing so had the known solution not been available. Furthermore, no data manipulation was preformed in the original, physical SSCP-I experiment nor recommended for numerically simulated results, although the present analysis suggests such considerations may be warranted

in future challenge problems.

5.4. Constant depth error

Finally, now, we are in a position to estimate the error in the constant depth assumption for post-processing of simulation data. In the previous analyses, as the depth increased beyond $\mathcal{D} = 2r_p$ the possibility of particles being obscured by other particles closer to the (synthetic) camera increases. Hence, the growth in error with $\mathcal{D}$, while certainly an error in the sense that it represents a disagreement between the measured values and the known values, becomes less and less a measure of the algorithmic error. In real, physical systems the depth is always full. The sharp cutoff is applied to the numerical predictions as a way to mimic the depth of view challenge with opaque particles.

While only approximate, we believe that the error in this methodology can be estimated by subtracting the L_2-norms at $\mathcal{D} = 2r_p$ as previously defined from modified L_2-norms computed using velocimetry measurements from $\mathcal{D}$ = full video and the (known) CFD-DEM data at $\mathcal{D} = 2r_p$. This difference in L_2-norms quantifies the additional error in using $\mathcal{D}$ = full video compared to the best possible scenario of using $\mathcal{D} = 2r_p$, which does not exist in the real world. The cut-off error is provided in Table 2 for all twelve quantities of interest considered previously. In some cases the additional error is almost negligible, specifically the standard deviation in the vertical velocity of both the time-series and probabilistic analysis. However in many metrics the error is non-negligible, on the order of 5%, often closer to 10%. By and large, the values in Table 2 indicate that particle flow modelers should not expect better than roughly 10% error compared to PTV data when post-

processed with a constant depth cut-off.

6. Summary, Conclusions, and Future Work

Particle tracking methods are a pervasive measurement technique in chemical engineering and related fields which utilize particle fluidization processes. While comparison with other measurement techniques has been studied [20], a method to assess the error in realistic data processed by PTV and related methods has not been performed. In this work, we borrow from a long standing concept in Particle Image Velocimetry (PIV) whereby photorealistic images or video is synthetically generated. This technique, commonly used in PIV challenge problems, may be used to directly quantify measurement error because the velocity fields underlying the manufactured data are known.

In this relatively novel study, known underlying data is taken from an MFiX CFD-DEM simulation, a Lagrangian particle method, of NETL's Small-scale Challenge Problem-I (SSCP-I). SSCP-I consists of a small, rectangular fluidized bed of (approximately) 3 mm particles. The data is rendered into a photorealistic scene using the open-source 3D creation software Blender [63]. Realistic light sources creating shadows are included, as are synthetic noise such as scratches on the face of the bed and fuzziness near the edges of the region of interest. Images from the scene are rendered into five 5.0 s replicate videos at 1000 Hz. To study the impact on the depth of field, the synthetic videos are generated by only considering particles within a specified distance from the inside of the front face: $\mathcal{D} = 1.5r_p$, $2r_p$, $3r_p$, $4r_p$, $6r_p$, $8r_p$, and the full bed depth ($\mathcal{D} \approx 46.8r_p$). Particles with centroid

depths $z_p > \mathcal{D}$ are masked from the underlying CFD-DEM dataset and not rendered in the scene at all.

The synthetic data are processed using three distinct velocimetry methods: Tracker, a pure PTV method; flowonthego, a pure optical flow velocimetry (OFV) method; and PTVResearch, a hybrid of the OFV and PTV schemes (see Sec. 4 for further description). The tracked velocities (i.e., a particle or feature) are binned into five square regions spanning the width of the bed at a prescribed height and post-processed using a time-series analysis (transient signals) and a probabilistic analysis (velocity distributions). Qualitative comparison between the known and measured data in the Supplementary Material indicates very good agreement when the depth of particles rendered into the synthetic video is restricted to $\mathcal{D} = 2r_p$. The time-series are quantified by their mean and standard deviation and the velocity PDFs by their mean, standard deviation, skewness and kurtosis. The error in the measurements are quantified by comparing averaged statistics from the measurements with the known data and summing into L_2-norms for each quantity of interest. The five replicate segments are used to compute confidence intervals (95% by t-test) for the error analyses. At $\mathcal{D} = 2r_p$, all methods give quantitatively accurate measurements. While this work is not intended to pit one method against another, the data did show that the pure PTV Tracker scheme provided the best results with this specific data-set with all but one of the twelve quantities of interest inside of 5% error, nine of them approximately 2% or less.

However, the error between the measured and known averaged quantities grows with the depth of field, $\mathcal{D}$. At full depth, the difference is appreciable,

often exceeding 20%. Yet this discrepancy does not (only) quantify the error in the algorithms; we do not expect the velocimetry methods to measure the velocity of particles which are obscured from the view of the camera by other particles closer to the face of the bed. To avoid this obvious error, it is common practice of modelers (particularly using numerical methods with Lagrangian particles) to consider only particles within a given distance of the bed face. The error in such an assumption can be estimated by considering a modified L_2-norm in which the full-bed depth video is taken for velocimetry measurement and compared to the CFD-DEM data at $\mathcal{D} = 2r_p$ and subtracting off the standard (one-to-one) L_2-norm at $\mathcal{D} = 2r_p$. The quantification of this "delta error," provided in Table 2, is an important benchmark for anyone performing numerical studies and comparing the results to velocimetry measurements. Even if the tracking method results are so accurate that they could be considered error free in themselves, an additional 5% to 10% error may be rolled up into the post-processing due to this simple assumption.

There is, of course, one obvious solution to avoiding some of this error: simply follow the present workflow and render the numerical solution into a photorealistic HSV and process it with the same velocimetry method. However, such an approach is almost certainly too cumbersome for most researchers. Useful future work might investigate how to minimize the error due to the constant cut-off depth of field in a more practical manner.

This work utilized three different velocimetry methods ranging from PTV to OFV. Rather than comparing one method against another, the three codes were used largely to ensure that the conclusions drawn from this study were not implementation nor method specific. The synthetic data in this case was

amenable to all three methods: the simulated experiment was simple (thin, rectangular), the rendering was relatively clean and the maximum particle displacements were rather small. It would be interesting in the future if the current workflow was used to push the extremes of the schemes to determine the robustness of the methods and, perhaps, find regions where different methods shine over others.

The use of HSVs and image processing will continue to be widely used techniques for extracting high quality information from multiphase flow experiments, especially as cameras continue to become cheaper and faster. It is imperative that practitioners understand the limitations of the optical experimental setups and validate their image processing algorithms with known solutions so that accurate results can be obtained and analysed. Without this validation step, results based on image processing are suspect. To help this community grow and facilitate validation of image processing codes, the authors are providing the HSV and processed known solutions from this work and are further working towards the release of blind PTV challenge problems to the community.

Acknowledgment

The authors would like to thank the developers of Blender and the Blender Foundation for providing the open-source rendering tool that enabled this work. This work was performed in support of the US Department of Energy's Fossil Energy Crosscutting Technology Research Program. The Research was executed through the NETL Research and Innovation Center's Advanced Reaction Systems Field Work Proposal. Research performed by

Leidos Research Support Team staff was conducted under the RSS contract 89243318CFE000003.

This work was funded by the Department of Energy, National Energy Technology Laboratory, an agency of the United States Government, through a support contract with Leidos Research Support Team (LRST). Neither the United States Government nor any agency thereof, nor any of their employees, nor LRST, nor any of their employees, makes any warranty, expressed or implied, or assumes any legal liability or responsibility for the accuracy, completeness, or usefulness of any information, apparatus, product, or process disclosed, or represents that its use would not infringe privately owned rights. Reference herein to any specific commercial product, process, or service by trade name, trademark, manufacturer, or otherwise, does not necessarily constitute or imply its endorsement, recommendation, or favoring by the United States Government or any agency thereof. The views and opinions of authors expressed herein do not necessarily state or reflect those of the United States Government or any agency thereof.

References

[1] D. o. Kunii, O. Levenspiel, Fluidization engineering, Butterworth-Heinemann series in chemical engineering, Butterworth-Heinemann, Boston, 2nd edition, 1991.

[2] D. Parker, C. Broadbent, P. Fowles, M. Hawkesworth, P. McNeil, Positron emission particle tracking-a technique for studying flow within engineering equipment, Nuclear Instruments and Methods in Physics Research Section A: Accelerators, Spectrometers, Detectors and Associated Equipment 326 (1993) 592–607.

[3] B. Hoomans, J. Kuipers, W. Briels, W. van Swaaij, Discrete particle simulation of bubble and slug formation in a two-dimensional gas-fluidised bed: a hard-sphere approach, Chemical Engineering Science 51 (1996) 99–118.

[4] J. Link, N. Deen, J. Kuipers, X. Fan, A. Ingram, D. Parker, J. Wood, J. Seville, PEPT and discrete particle simulation study of spout-fluid bed regimes, AIChE journal 54 (2008) 1189–1202.

[5] D. J. Holland, C. R. Müller, J. S. Dennis, L. F. Gladden, A. J. Sederman, Spatially resolved measurement of anisotropic granular temperature in gas-fluidized beds, Powder Technology 182 (2008) 171–181.

[6] C. R. Müller, D. J. Holland, A. J. Sederman, S. A. Scott, J. S. Dennis, L. F. Gladden, Granular temperature: comparison of magnetic resonance measurements with discrete element model simulations, Powder Technology 184 (2008) 241–253.

[7] A. Penn, T. Tsuji, D. O. Brunner, C. M. Boyce, K. P. Pruessmann, C. R. Müller, Real-time probing of granular dynamics with magnetic resonance, Science Advances 3 (2017) e1701879.

[8] H. Wang, W. Yang, Application of electrical capacitance tomography in circulating fluidised beds–a review, Applied Thermal Engineering (2020) 115311.

[9] J. M. Weber, J. S. Mei, Bubbling fluidized bed characterization using electrical capacitance volume tomography (ecvt), Powder Technology 242 (2013) 40 – 50. Selected Papers from the 2010 NETL Multiphase Flow Workshop.

[10] J. M. Weber, M. M. Bobek, R. W. Breault, J. S. Mei, L. J. Shadle, Investigation of core-annular flow in an industrial scale circulating fluidized bed riser with electrical capacitance volume tomography (ecvt), Powder technology 327 (2018) 524–535.

[11] J. Link, C. Zeilstra, N. Deen, H. Kuipers, Validation of a discrete particle model in a 2d spout-fluid bed using non-intrusive optical measuring techniques, The Canadian Journal of Chemical Engineering 82 (2004) 30–36.

[12] J. Jung, D. Gidaspow, I. K. Gamwo, Measurement of two kinds of granular temperatures, stresses, and dispersion in bubbling beds, Industrial & Engineering Chemistry Research 44 (2005) 1329–1341.

[13] J. A. Laverman, I. Roghair, M. v. S. Annaland, H. Kuipers, Investigation into the hydrodynamics of gas–solid fluidized beds using particle image

velocimetry coupled with digital image analysis, The Canadian Journal of Chemical Engineering 86 (2008) 523–535.

[14] X.-L. Zhao, S.-Q. Li, G.-Q. Liu, Q. Song, Q. Yao, Flow patterns of solids in a two-dimensional spouted bed with draft plates: Piv measurement and dem simulations, Powder Technology 183 (2008) 79–87.

[15] M. S. van Buijtenen, W.-J. van Dijk, N. G. Deen, J. Kuipers, T. Leadbeater, D. Parker, Numerical and experimental study on multiple-spout fluidized beds, Chemical Engineering Science 66 (2011) 2368–2376.

[16] M. S. van Buijtenen, M. Börner, N. G. Deen, S. Heinrich, S. Antonyuk, J. Kuipers, An experimental study of the effect of collision properties on spout fluidized bed dynamics, Powder Technology 206 (2011) 139–148.

[17] B. Gopalan, F. Shaffer, A new method for decomposition of high speed particle image velocimetry data, Powder technology 220 (2012) 164–171.

[18] B. Gopalan, F. Shaffer, Higher order statistical analysis of eulerian particle velocity data in cfb risers as measured with high speed particle imaging, Powder technology 242 (2013) 13–26.

[19] F. Shaffer, B. Gopalan, R. W. Breault, R. Cocco, S. R. Karri, R. Hays, T. Knowlton, High speed imaging of particle flow fields in cfb risers, Powder technology 242 (2013) 86–99.

[20] T. Hagemeier, M. Börner, A. Bück, E. Tsotsas, A comparative study on optical techniques for the estimation of granular flow velocities, Chemical Engineering Science 131 (2015) 63–75.

[21] T. Hagemeier, C. Roloff, A. Bück, E. Tsotsas, Estimation of particle dynamics in 2-d fluidized beds using particle tracking velocimetry, Particuology 22 (2015) 39–51.

[22] B. Gopalan, M. Shahnam, R. Panday, J. Tucker, F. Shaffer, L. Shadle, J. Mei, W. Rogers, C. Guenther, M. Syamlal, Measurements of pressure drop and particle velocity in a pseudo 2-D rectangular bed with Geldart Group D particles, Powder Technology 291 (2016) 299–310.

[23] K. Vollmari, R. Jasevičius, H. Kruggel-Emden, Experimental and numerical study of fluidization and pressure drop of spherical and non-spherical particles in a model scale fluidized bed, Powder Technology 291 (2016) 506–521.

[24] A. Carlos Varas, E. Peters, J. Kuipers, Experimental study of full field riser hydrodynamics by piv/dia coupling, Powder technology 313 (2017) 402–416.

[25] A. Carlos Varas, E. Peters, J. Kuipers, Cfd-dem simulations and experimental validation of clustering phenomena and riser hydrodynamics, Chemical Engineering Science 169 (2017) 246–258.

[26] Z. Jiang, T. Hagemeier, A. Bueck, E. Tsotsas, Experimental measurements of particle collision dynamics in a pseudo-2d gas-solid fluidized bed, Chemical Engineering Science 167 (2017) 297–316.

[27] K. Meyer, A. Bück, E. Tsotsas, Determination of particle exchange rates at over-flow weirs in horizontal fluidised beds by particle tracking velocimetry, Particuology 32 (2017) 1–9.

[28] H. Zhang, M. Liu, T. Li, Z. Huang, X. Sun, H. Bo, Y. Dong, Experimental investigation on gas-solid hydrodynamics of coarse particles in a two-dimensional spouted bed, Powder Technology 307 (2017) 175–183.

[29] W. D. Fullmer, C. Q. LaMarche, A. Issangya, P. Liu, R. Cocco, C. M. Hrenya, Experimental data for code validation: Horizontal air jets in a semicircular fluidized bed of geldart group d particles, AIChE Journal 64 (2018) 2351–2363.

[30] Z. Jiang, T. Hagemeier, A. Bück, E. Tsotsas, Color-ptv measurement and cfd-dem simulation of the dynamics of poly-disperse particle systems in a pseudo-2d fluidized bed, Chemical Engineering Science 179 (2018) 115–132.

[31] T. Li, H. Zhang, M. Liu, Z. Huang, H. Bo, Y. Dong, Experimental investigation on vertical plug formation of coarse particles by a non-mechanical feeder, Powder technology 338 (2018) 692–701.

[32] W. D. Fullmer, J. E. Higham, C. Q. LaMarche, A. Issangya, R. Cocco, C. M. Hrenya, Comparison of velocimetry methods for horizontal air jets in a semicircular fluidized bed of geldart group d particles, Powder Technology 359 (2020) 323–330.

[33] J. JHigham, M. Shahnam, A. Vaidheeswaran, Using a proper orthogonal decomposition to elucidate features in granular flows, Granular Matter (2020).

[34] E. Azanza, F. Chevoir, P. Moucheront, Experimental study of collisional

granular flows down an inclined plane, Journal of Fluid Mechanics 400 (1999) 199–227.

[35] D. M. Hanes, O. R. Walton, Simulations and physical measurements of glass spheres flowing down a bumpy incline, Powder Technology 109 (2000) 133–144.

[36] A. Armanini, H. Capart, L. Fraccarollo, M. Larcher, Rheological stratification in experimental free-surface flows of granular–liquid mixtures, Journal of Fluid Mechanics 532 (2005) 269–319.

[37] P. Jop, Y. Forterre, O. Pouliquen, Crucial role of sidewalls in granular surface flows: consequences for the rheology, Journal of Fluid Mechanics 541 (2005) 167–192.

[38] S. P. Pudasaini, K. Hutter, S.-S. Hsiau, S.-C. Tai, Y. Wang, R. Katzenbach, Rapid flow of dry granular materials down inclined chutes impinging on rigid walls, Physics of Fluids 19 (2007) 053302.

[39] C. Slominski, M. Niedostatkiewicz, J. Tejchman, Application of particle image velocimetry (piv) for deformation measurement during granular silo flow, Powder Technology 173 (2007) 1–18.

[40] S. K. Bryant, W. A. Take, E. T. Bowman, Observations of grain-scale interactions and simulation of dry granular flows in a large-scale flume, Canadian Geotechnical Journal 52 (2014) 638–655.

[41] C. Q. LaMarche, J. S. Curtis, Cratering of a particle bed by a subsonic turbulent jet: Effect of particle shape, size and density, Chemical Engineering Science 138 (2015) 432–445.

[42] D. Gollin, W. Brevis, E. T. Bowman, P. Shepley, Performance of piv and ptv for granular flow measurements, Granular Matter 19 (2017) 42.

[43] J. Higham, P. Shepley, M. Shahnam, Measuring the coefficient of restitution for all six degrees of freedom, Granular Matter 21 (2019) 15.

[44] O. Ayeni, C. Wu, K. Nandakumar, J. Joshi, Development and validation of a new drag law using mechanical energy balance approach for dem–cfd simulation of gas–solid fluidized bed, Chemical Engineering Journal 302 (2016) 395–405.

[45] Y. Tsuji, T. Tanaka, S. Yonemura, Particle induced turbulence, Appl. Mech. Rev. 47 (1994) 75–79.

[46] M. van der Hoef, M. van Sint Annaland, N. Deen, J. Kuipers, Numerical simulation of dense gas-solid fluidized beds: A multiscale modeling strategy, Annual Review of Fluid Mechanics 40 (2008) 47–70.

[47] S. Tenneti, S. Subramaniam, Particle-resolved direct numerical simulation for gas-solid flow model development, Annual Review of Fluid Mechanics 46 (2014) 199–230.

[48] H. Zhu, Z. Zhou, R. Yang, A. Yu, Discrete particle simulation of particulate systems: theoretical developments, Chemical Engineering Science 62 (2007) 3378–3396.

[49] J. Capecelatro, O. Desjardins, An euler-lagrange strategy for simulating particle-laden flows, Journal of Computational Physics 238 (2013) 1–31.

[50] S. Patankar, Numerical heat transfer and fluid flow, Hemisphere Pub. Corp., McGraw-Hill, Washington, New York, 1980.

[51] M. Syamlal, MFIX documentation: Numerical technique, Technical Report DOE/MC31346-5824, U.S. Department of Energy, 1998.

[52] D. Liu, B. van Wachem, Comprehensive assessment of the accuracy of cfd-dem simulations of bubbling fluidized beds, Powder Technology 343 (2019) 145–158.

[53] L. Lu, B. Gopalan, S. Benyahia, Assessment of different discrete particle methods ability to predict gas-particle flow in a small-scale fluidized bed, Industrial & Engineering Chemistry Research 56 (2017) 7865–7876.

[54] H. A. Elghannay, D. K. Tafti, Dem predictions of netl small scale challenge problem, in: ASME 2014 4th Joint US-European Fluids Engineering Division Summer Meeting, American Society of Mechanical Engineers, p. V01CT23A001.

[55] G. Bradski, The OpenCV Library, Dr. Dobb's Journal of Software Tools (2000).

[56] S. van der Walt, S. C. Colbert, G. Varoquaux, The numpy array: A structure for efficient numerical computation, Computing in Science Engineering 13 (2011) 22–30.

[57] P. Virtanen, R. Gommers, T. E. Oliphant, M. Haberland, T. Reddy, D. Cournapeau, E. Burovski, P. Peterson, W. Weckesser, J. Bright, S. J. van der Walt, M. Brett, J. Wilson, K. Jarrod Millman, N. Mayorov, A. R. J. Nelson, E. Jones, R. Kern, E. Larson, C. Carey, İ. Polat,

Y. Feng, E. W. Moore, J. Vand erPlas, D. Laxalde, J. Perktold, R. Cimrman, I. Henriksen, E. A. Quintero, C. R. Harris, A. M. Archibald, A. H. Ribeiro, F. Pedregosa, P. van Mulbregt, S. . . Contributors, SciPy 1.0: Fundamental Algorithms for Scientific Computing in Python, Nature Methods 17 (2020) 261–272.

[58] C. Cierpka, B. Lütke, C. J. Kähler, Higher order multi-frame particle tracking velocimetry, Experiments in Fluids 54 (2013) 1533.

[59] J. J. Gibson, The perception of the visual world., Houghton Mifflin, Boston, 1950.

[60] B. D. Lucas, T. Kanade, An iterative image registration technique with an application to stereo vision, in: Proceedings of the 7th International Joint Conference on Artificial Intelligence (IJCAI), Vancouver, BC Canada, Aug. 24–28, 1981, pp. 121–130.

[61] B. D. Lucas, Generalized image matching by the method of differences, Ph.D. thesis, Carnegie Mellon University, 1985.

[62] D. G. Goring, V. I. Nikora, Despiking acoustic doppler velocimeter data, Journal of hydraulic engineering 128 (2002) 117–126.

[63] B. O. Community, Blender - a 3D modelling and rendering package, Blender Foundation, Stichting Blender Foundation, Amsterdam, 2020.

Table 1: The 95^{th}-percentile of the instantaneous discrepancy of the time-series velocity measurement at a cut-off depth of $\mathcal{D} = 2r_p$.

Tracker					
δu_{95}	1.5	3.2	4.5	3.1	1.3
δv_{95}	5.2	4.6	5.6	4.3	4.2
PTVResearch					
δu_{95}	5.6	9.8	12.4	8.9	4.8
δv_{95}	12.1	4.3	5.2	4.3	13.2
flowonthego					
δu_{95}	2.9	8.9	12.2	9.0	4.0
δv_{95}	4.4	7.2	9.3	11.7	15.3

Table 2: Approximate error incurred by assuming a constant depth of $\mathcal{D} = 2r_p$ in the CFD-DEM data.

statistic	Tracker	PTVResearch	flowonthego
U	6.36 ± 2.41	2.88 ± 11.57	3.55 ± 3.33
V	0.74 ± 1.83	± 6.35	1.02 ± 1.14
u'	5.20 ± 2.04	2.03 ± 1.69	4.27 ± 2.89
v'	1.00 ± 1.12	0.60 ± 1.92	1.12 ± 1.25
μ_u	8.74 ± 6.47	6.85 ± 8.18	9.01 ± 10.42
μ_v	2.17 ± 2.01	0.93 ± 4.98	4.73 ± 2.38
σ_u	11.46 ± 2.74	4.99 ± 2.54	13.62 ± 4.19
σ_v	1.62 ± 1.66	0.88 ± 1.25	3.98 ± 2.39
γ_u	21.71 ± 13.37	18.92 ± 30.37	22.43 ± 15.93
γ_v	12.36 ± 7.85	13.42 ± 11.66	11.86 ± 14.27
κ_u	7.94 ± 3.46	7.89 ± 9.21	-
κ_v	2.92 ± 2.05	5.35 ± 2.39	3.51 ± 2.25

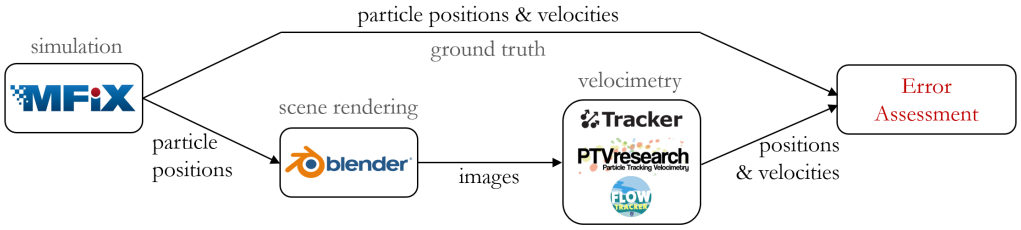

Figure 1: Flowchart outlining the novel workflow of this study.

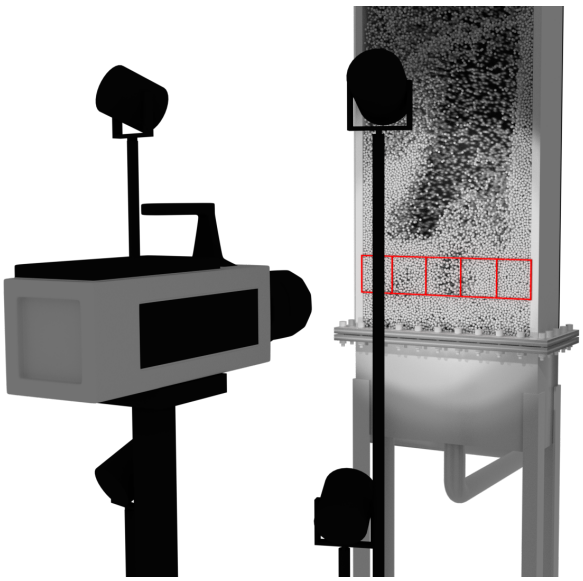

Figure 2: Rendering of the virtual experiment, showing the model bed containing near-wall particles (white), the camera and its orientation pointing towards the region of interest (red boxes) and the orientation and spread of the four surrounding light sources.

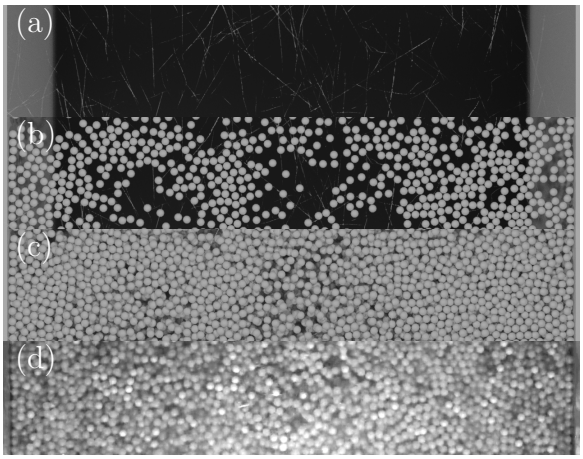

Figure 3: Example renderings of the scene: (a) without particles, highlighting scratches on front acrylic wall, (b) first frame of the $1.5r_p$ case in which only particles with centroids within a distance of $1.5r_p$ from the wall are visible, (c) the same first frame of the full case when all particles are considered, and (d) an example taken from the real SSCP HSV used for particle tracking.

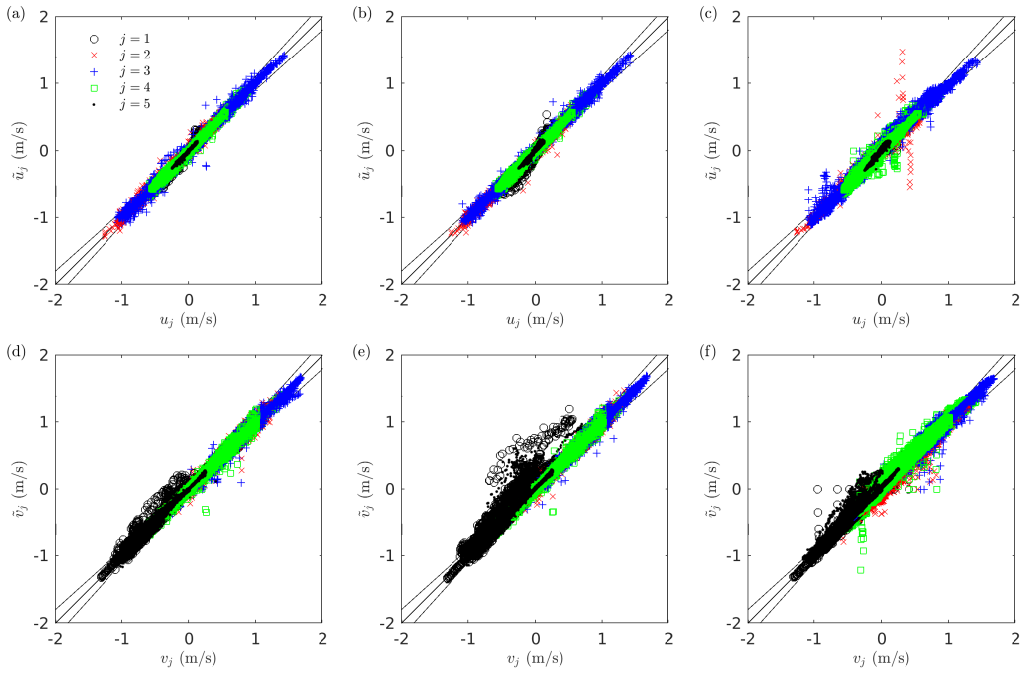

Figure 4: Parity plots comparing the instantaneous u- (a, b, c), and v-velocity (d, e, f) components measured by Tracker (a, d), PTVResearch (b, e), and flowonthego (c, f) to the known CFD-DEM solution at a cut-off depth of $\mathcal{D} = 2r_p$.

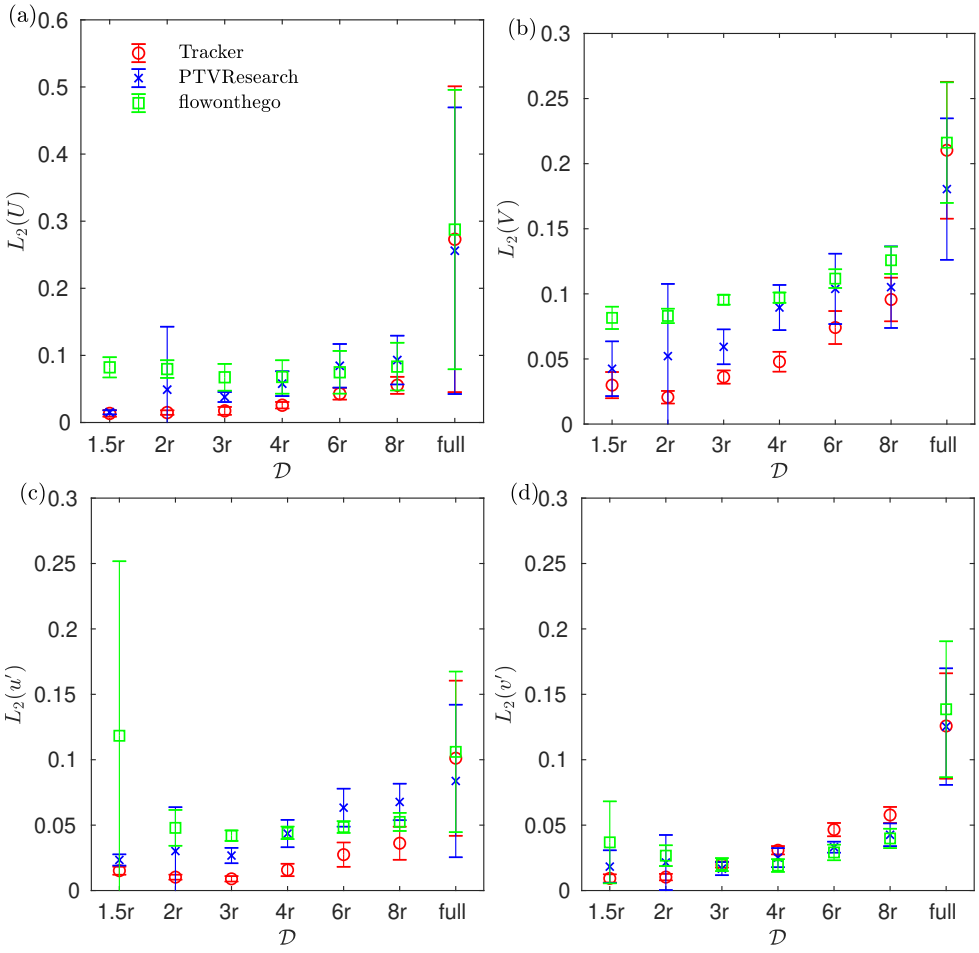

Figure 5: L_2-norm of measurement error as a function of imaging cut-off depth, $\mathcal{D}$, of the mean (a, b) and standard deviation (c, d) of the time-series analysis of the u- (a, c), and v-velocity (b, d) components.

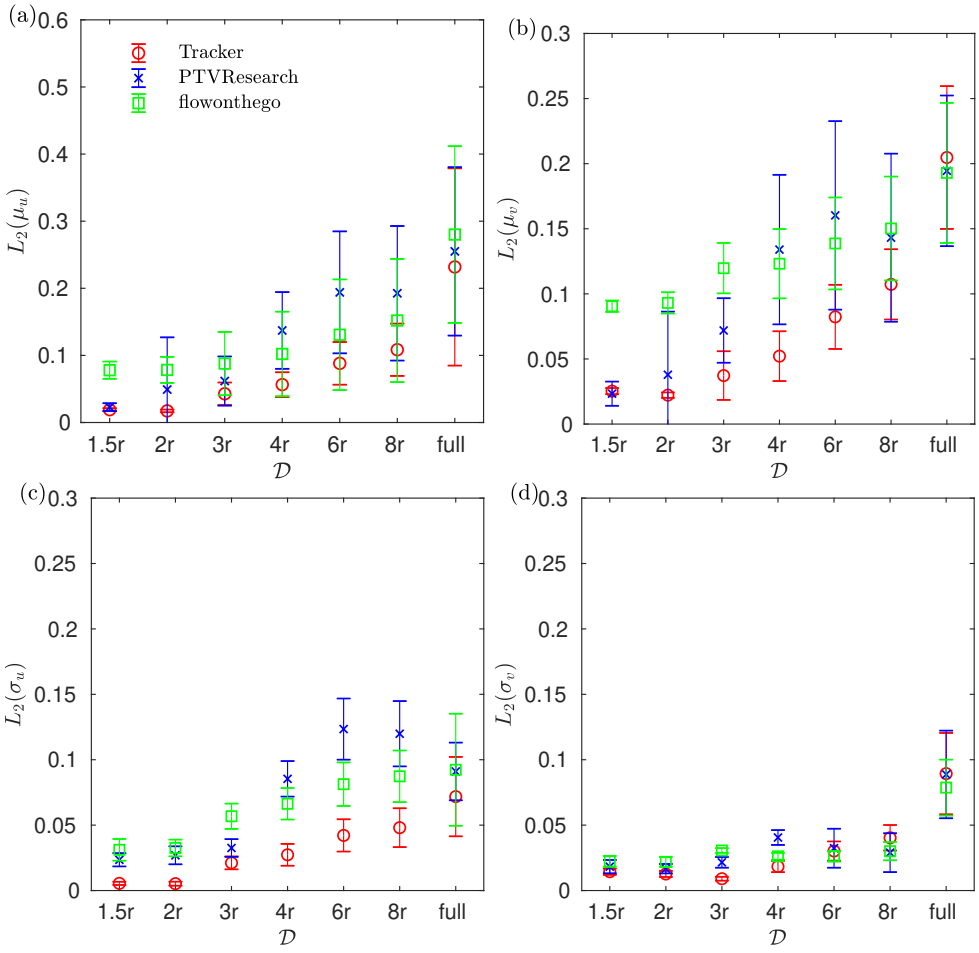

Figure 6: L_2-norm of measurement error as a function of imaging cut-off depth, $\mathcal{D}$, of the mean (a, b) and standard deviation (c, d) of the probability distribution analysis of the u- (a, c), and v-velocity (b, d) components.

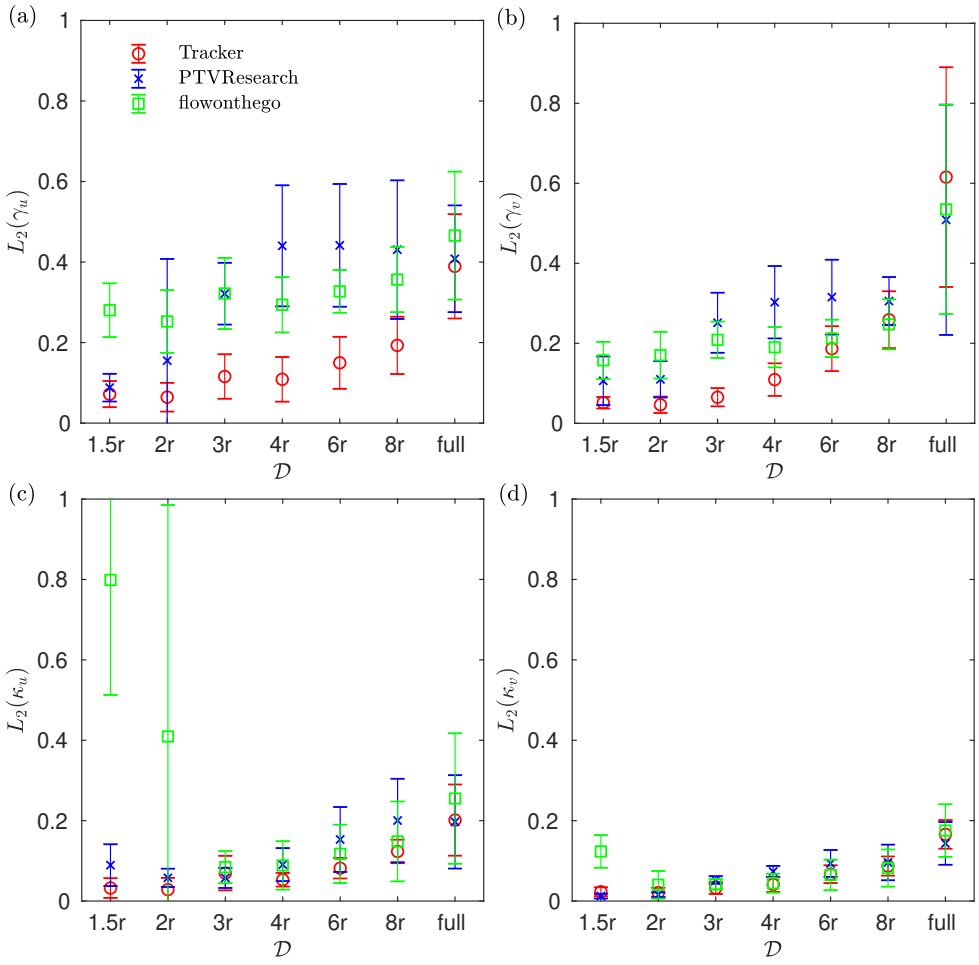

Figure 7: L_2-norm of measurement error as a function of imaging cut-off depth, $\mathcal{D}$, of the skewness (a, b) and kurtosis (c, d) of the probability distribution analysis of the u- (a, c), and v-velocity (b, d) components.